Supplementary Materials for

Self-Catalytic Membrane Photo-Reactor made of Carbon Nitride Nanosheets

Kai-Ge Zhou,[a] Daryl McManus,[a] Eric Prestat,[b] Xing Zhong,[c] Yuyoung Shin,[a] Hao-Li Zhang,[d] Sarah Haigh[b] and Cinzia Casiraghi*[a]*

[a] *School of Chemistry, University of Manchester, Oxford Road, Manchester, M13 9PL, UK*

[b] *School of Materials, University of Manchester, Oxford Road, Manchester, M13 9PL, UK*

[c] *College of Chemical Engineering and Materials Science, Zhejiang University of Technology, Hangzhou 310014, China*

[d] *State Key Laboratory of Applied Organic Chemistry, Lanzhou University, China*

[*] *Corresponding authors:* cinzia.casiraghi@manchester.ac.uk; *zhkg7120@163.com*

S1. Material preparation

S1.1 Semi-empirical theory for the liquid exfoliation in binary solvents system

Recently, Coleman et al developed a method to evaluate the exfoliation ability of a non-electrolytic individual solvent in dispersing a layered material.[1] The concentration of 2D crystals dispersed in the solvent, *C*, depends on a group of parameters related to solute and solvent[1b]:

$$C \propto \exp\{-\frac{\bar{v}}{RT}\left[\left(\delta_{D,solv}-\delta_{D,solu}\right)^2+\left(\delta_{P,solv}-\delta_{P,solu}\right)^2/4+\left(\delta_{H,solv}-\delta_{H,solu}\right)^2/4\right]\} \quad (1)$$

$$R_a=[4\left(\delta_{D,solv}-\delta_{D,solu}\right)^2+\left(\delta_{P,solv}-\delta_{P,solu}\right)^2+\left(\delta_{H,solv}-\delta_{H,solu}\right)^2]^{0.5} \quad (2)$$

where $\bar{v}$ is the volume per mole of the 2D nanosheets, R is Boltzmann constant, T is absolute temperature. The two parameters δ_{solv} and δ_{solu} are the Hansen' solubility parameters (HSP) that describe the nature of solvent and solute, respectively; the subscript D, P and H correlates with dispersive, polar and hydrogen bonding, respectively.

The HSP theory has been extended to solvents mixture.[2] Instead of the solubility parameters for each individual solvent, here the HSP values are a combination of every compound ($\delta_{compound,N}$) for its volume ratio (φ_N):

$$\delta_{mix}=\sum_k\left(\varphi_N\delta_{compound,N}\right) \quad (3)$$

In a two-solvent system, Eq. 3 becomes:

$$\delta_{solv}=\varphi_{N1}\delta_{N1}+\varphi_{N2}\delta_{N2}=\varphi_{N1}\delta_{N1}+(1-\varphi_{N1})\delta_{N2}=\varphi_{N1}(\delta_{N1}-\delta_{N2})+\delta_{N2} \quad (4)$$

In our previous work,[2] we combined Eq. 4 into Eq. 2 relying on the HSP values reported for 2D nanosheets.[1c] However, the HSP values are known only for a small selection of 2D crystals[1b, 1c, 3], and they are not known for g-C_3N_4. In order to optimize the solvent mixture for g-C_3N_4 without knowing the HSP values, we used the following method. By taking Eq. 4 into Eq. 1, the concentration can be written as:

$$C \propto \exp\{-\frac{\bar{v}}{RT}\left[\left(\varphi_{N1}(\delta_{D,N1}-\delta_{D,N2})+\delta_{D,N2}-\delta_{D,solu}\right)^2+\left(\varphi_{N1}(\delta_{P,N1}-\delta_{P,N2})+\delta_{P,N2}-\delta_{P,solu}\right)^2/ 4+\left(\varphi_{N1}(\delta_{H,N1}-\delta_{H,N2})+\delta_{H,N2}-\delta_{H,solu}\right)^2/4\right]\} \quad (5)$$

In the right side of Eq. 5, the volume ratio of a composite solvent (φ_{N1}) is the only variable (the HSP values are constants). If we take the natural logarithmic form of both side of Eq. 5, we can demonstrate that *lnC* obeys a second-order polynomial relation on the volume ratio, φ_{N1}:

$$\ln C = A + B\varphi_{N1} + C{\varphi_{N1}}^2 \quad (6)$$

where:

$$B = -\frac{2\bar{v}}{RT}[(\delta_{D,N1} - \delta_{D,N2})(\delta_{D,N2} - \delta_{D,solu}) + 0.25(\delta_{P,N1} - \delta_{P,N2})(\delta_{P,N2} - \delta_{P,solu}) + 0.25(\delta_{D,N1} - \delta_{D,N2})(\delta_{D,N2} - \delta_{D,solu})] \quad (7)$$

$$C = -\frac{\bar{v}}{RT}[(\delta_{D,N1} - \delta_{D,N2})^2 + 0.25(\delta_{P,N1} - \delta_{P,N2})^2 + 0.25(\delta_{H,N1} - \delta_{H,N2})^2] \quad (8)$$

and A is another constant. A, B, C are independent on the solvent ratio. As we do not know the coefficient of the right side in Eq. 5, the accurate value of the intercept A cannot be directly known. However, if we have a few (more than three) experimental results relating concentration and solvent ratio, then we can semi-empirically identify the constants A, B and C. In particular, when φ_{N1} equals -B/2C, the concentration reaches a maximum, so we assign the value of –B/2C as φ_{max}.

S1.2 Preparation of the g-C_3N_4 suspensions

The bulk phase of g-C_3N_4 was synthesized by the thermal treatment of melamine at 600 ℃ for 1.5 hours.[4] 30 mg of g-C_3N_4 bulk was mixed with 10 mL isopropanol (IPA) and water. The soya-like suspension was mild sonicated in a bath cleaner (DAWE 6290A, 150W, 25 kHz) for 12 hours to obtain the dispersion of g-C_3N_4 nanosheets. The bulk residual was removed by centrifugation at 1000 rpm (~79g) for 10 min. To further separate the thin layers g-C_3N_4, the supernatant (top 2/3) obtained in the last process was then centrifuged at 3000 rpm (~664g) for 10 min. The top 1/2 supernatant of g-C_3N_4 was collected for characterization. To avoid the signal overflow, 0.5mL of this dispersion was diluted ten times by the corresponding solvent mixture for UV-Vis absorption measurements (Cary 300, Varian Inc.). The main absorption peak of g-C_3N_4 appears at 322nm, with a shoulder at 400 nm, Figure 1b, similar to a previous report. [5] As the melamine and its derivatives absorb only below 260 nm,[6] residual of the precursor can be distinguished from the bulk by UV-Vis absorption measurements. The corresponding blank IPA/H_2O solvent mixture was then used to correct the baseline of each dispersion.

We applied the semi-empirical method described in S1.1 to LPE of g-C_3N_4. The volume ratio of IPA was increased from 0 to 100% in steps of 10%. The soya-like g-C_3N_4 dispersions obtained at different solvents ratio are shown in Figure 1(a). One can immediately note by eyes that the g-C_3N_4 dispersion in the IPA/H_2O mixture has higher concentration than that one obtained in either IPA or water only. As the absorbance of 2D nanosheets obeys Lambert-Beer law, the absorbance is proportional to the concentration of g-C_3N_4. Therefore, we can simply use the absorbance at 322 nm to evaluate the changes in concentration with the solvent ratio, Figure S1(b). Figure S1(c) shows the natural logarithm of absorbance as a function of the solvent ratio. The highest concentration appears at ~50 vol% IPA. By fitting the experimental curve with Eq. 6, we found φ_{max} = 44 vol%, in good agreement with the experimental results (~50 vol%). From a mathematical point of view, there is no increase in the accuracy of φ_{max} when using more than three or four experimental points (Figure S1(c,d) vs Figure 1 main text, where 10 points have been used), so just a few exfoliation experiments are needed to quickly optimize the solvent ratio to get the highest concentration. The dispersions of g-C_3N_4 used for photo-degradation studies where obtained by using 50vol% IPA/H_2O in order to obtain highly concentrated and stable material.

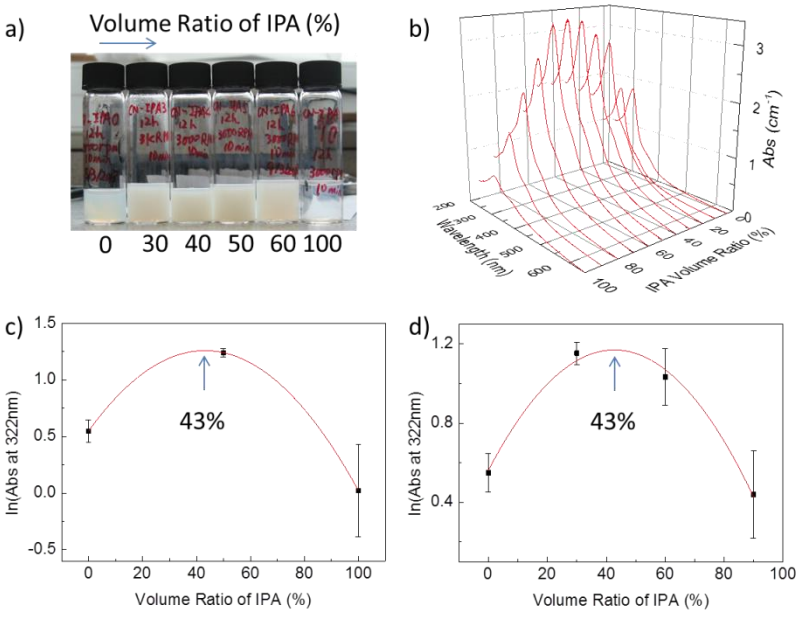

Figure S1 (a) Pictures of the g- C_3N_4 dispersions obtained with different IPA volume ratio; (b) UV-Vis spectra of dispersed g-C_3N_4 in IPA/H_2O mixtures with different IPA volume ratio (diluted 10 times); c) use of our semi-empirical method to calculate the optimum IPA volume ratio. Example with 3 (c) and 4 (d) experimental points is given to show that there is not improvement in accuracy above 3 points.

S1.3 Preparation of the g-C_3N_4 laminates

The g-C_3N_4 dispersions obtained by using 50vol% IPA/H_2O were filtrated and deposited on an anodic alumina oxide membrane (pore size=20nm, diameter=25mm, Whatsman Inc.). The results in Fig. 2B (main text) have been obtained by calculating the weight of the laminate from the concentration and total volume. Scheme S1 shows a schematic and a picture of the vacuum filtration setup used to produce the membrane. We remark that the pore size of the alumina disk is well smaller than the average size of the flakes (S2.2).

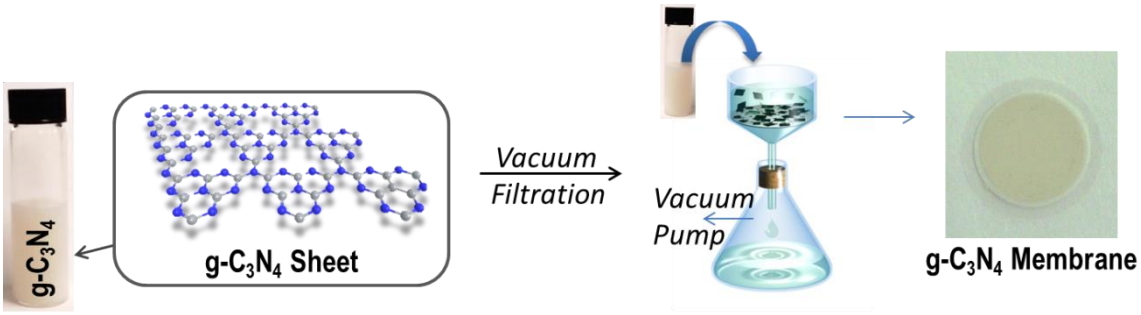

Scheme S1 the fabrication process of the g-C_3N_4 membranes.

S2. Characterization

S2.1 UV-Vis absorption

UV-Vis absorption measurements were carried out as described in S1. To identify the absorption coefficient, 50mL g-C_3N_4 dispersion in 50vol% IPA/H_2O was filtered by an anodic alumina oxide membrane (pore size=0.02µm, from Millipore). The free-standing laminate was dried overnight at 100 °C to remove the solvent, before being weighted to calculate the absorption coefficient. We found that the absorption coefficient of g-C_3N_4 at 322nm is 4800 mL mg^{-1} m^{-1}.

S2.2 Atomic Force Microscopy (AFM)

The as-prepared g-C_3N_4 dispersion was diluted below 0.001mg/mL to avoid aggregation; 20 µL of the diluted dispersion was drop-casted on a freshly cleaved mica surface and dried under ambient conditions. The AFM images were collected by a Multidimension, Veeco, using tapping mode. A setpoint of 362.69 mV (~220nN) was applied to the tip. The scanning rate was set to 15µm/s. The height of over

50 g-C_3N_4 flakes was measured to determine statistical height distribution. We found that the thickness of the nanosheets is mainly distributed between 4-6 nm (Fig S2c), however, we could observe also thinner nanosheets below 1 nm thickness (ie. less than 3 layers), as shown in Fig S2b. Generally, over 90 % flakes are less than 10 nm thick (Fig. S2c), confirming successful exfoliation.

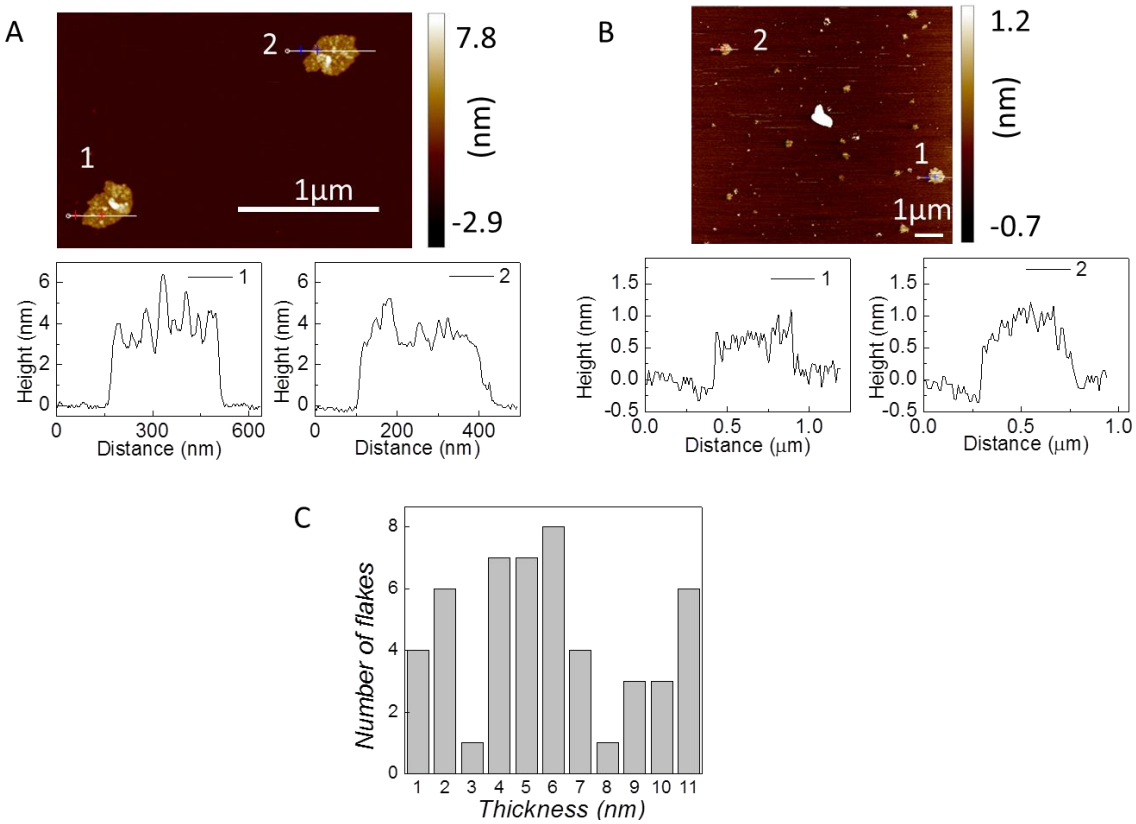

Figure S2 (a) AFM image of two g-C_3N_4 nanosheets and their corresponding cross section heights. The thickness is ~3-6 nm and lateral size is ~300nm; (b) AFM image of two thinner g-C_3N_4 nanosheets and their corresponding cross section heights. The thickness is ~0.6-1nm and lateral size is ~500nm. ; c) Statistical analysis of the g-C_3N_4 sheet thickness distribution measured by AFM.

S2.3 X-Ray Diffraction

The crystalline phases of the precursor melamine, g-C_3N_4 bulk (in powder) and the laminate were identified by using a powder X-ray diffractometer (XRD, RINT2100; Rigaku, Japan) with monochromated CuKα radiation. The applied voltage and current to the Cu target were 40 kV and 40 mA, respectively. The interlayer distance of the synthesized g-$C_3N_4$was calculated using the Bragg equation.

S2.4 Solid and liquid NMR

^{13}C CP-MAS solid-state NMR spectra was recorded at ambient temperature on the conventional pulsed spectrometer DSX Avance 500 (Bruker) operating at a resonance frequency of 500 MHz. The samples were contained in 4-mm ZrO_2 rotors, which were mounted in standard double-resonance MAS probes (Bruker). For each compound, 100mg solid sample was carefully grinded and then tightly filled into the rotor. The dispersion of g-C_3N_4 was filtrated to collect 100 mg laminate and grinded for solid NMR measurement. The operation conditions follows the instruction in previous reference.[7] In case of melamine, additional liquid NMR was recorded using a Bruker DRX-400 MHz NMR spectrometer at room temperature (d^6-DMSO was used to dissolve melamine).

Figure S3 shows the ^{13}C-NMR spectra of melamine precursor (solid and liquid), g-C_3N_4 bulk and laminate. The chemical shifts for melamine precursor and bulk and laminate of g-C_3N_4 are listed in Table S1, including the reference chemical shift for melamine. The liquid-NMR spectrum of melamine shows only a single peak, while the solid-NMR spectrum shows a close pair of peaks at 168.8 and 167.6 ppm, due to tautomerization. [7] After thermal treatment, the solid NMR signals are further split into two groups. In the first group, a couple of peaks located at 164 and 162 ppm, corresponding to the carbon connected to the vertex amine (α position), are seen. It is noted that the chemical shifts of this couple are lower than those in melamine in similar chemical environment. The possible reason is that the extended aromatic structure in the unit of tri-s-triazine provides more shielding effect on α-carbon. Moreover, a new group of peaks appears at 156 and 157 ppm, corresponding to the carbon at the side (β position). The chemical shifts of the g-C_3N_4 laminate are similar to its bulk phase. Our results are similar to the ones of the model molecule, tri-s-triazine, which has the same skeleton as one unite of g-C_3N_4. [7]

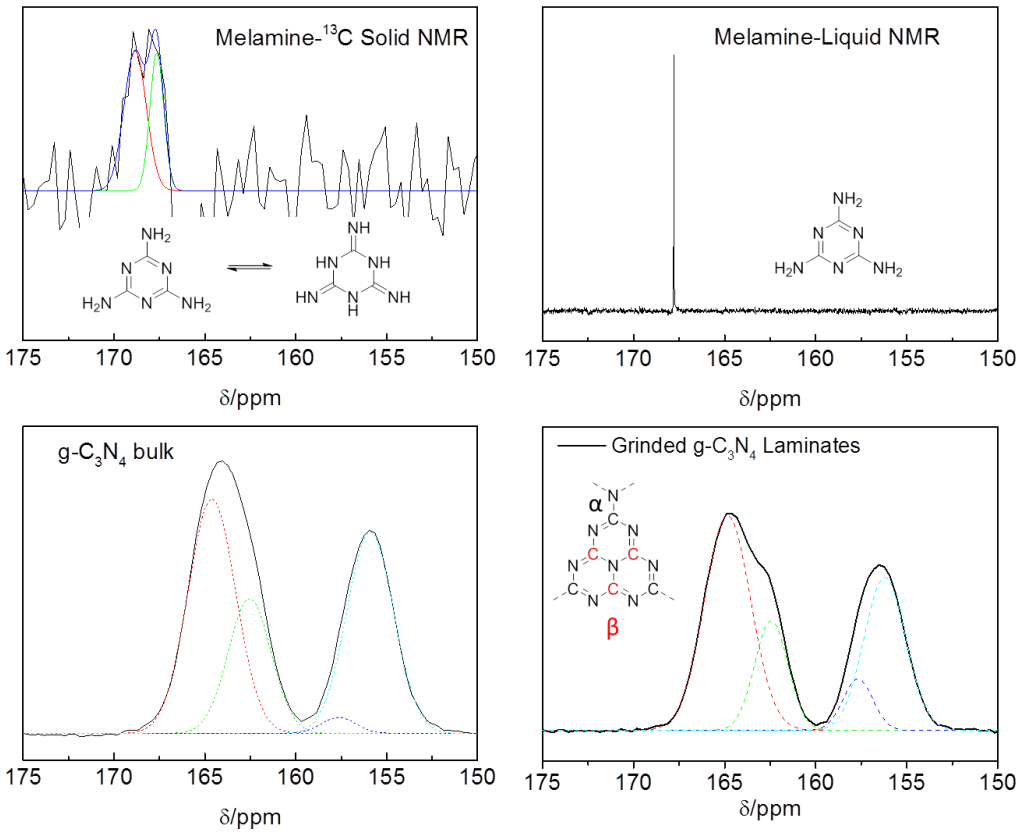

Figure S3 The ^{13}C-NMR spectrum of melamine precursor (solid and liquid), g-C_3N_4 bulk and laminate.

Table S1. ^{13}C-NMR chemical shifts of precursor and g-C_3N_4 bulk and laminate, as compared to melamine and tris-s-triazine references. [7] *Liquid NM is indicated by the letter "l". In all other cases, solid NMR has been used.*

^{13}C	δ(α)/ppm	δ(β)/ppm
Melamine	168.8;167.6	
Melamine (l)	167.7	
Ref. Melamine	169.2;167.5	
Ref. Melamine (l)	167.1	
g-C_3N_4 Bulk	164.6;162.5	157.6;155.9
g-C_3N_4 Laminate	164.8; 162.4	157.7; 156.2
Ref. Tris-s-triazine	166.4; 164.3	156.0; 155.1

S2.5 Scanning Electron Microscopy (SEM)

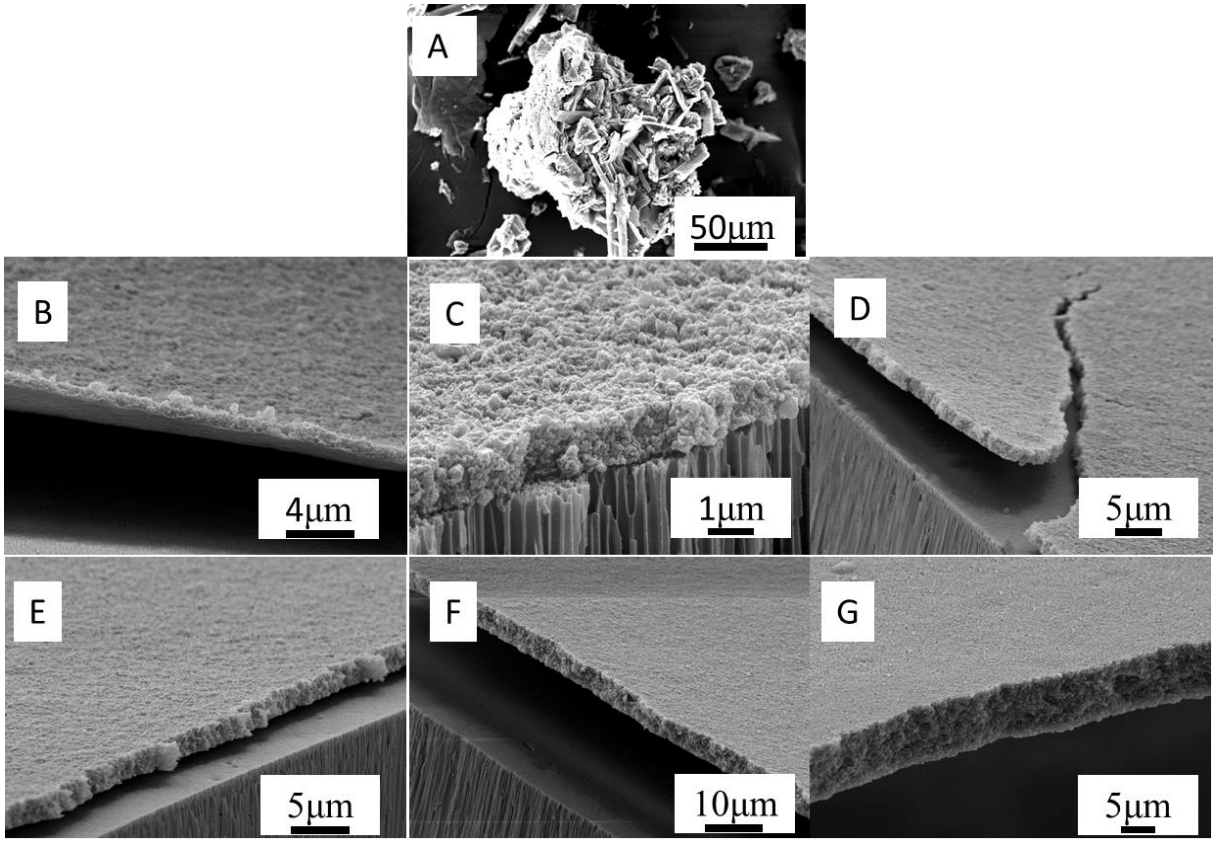

Figure S4. SEM images of g-C_3N_4 bulk (A) and the cross section images of the g-C_3N_4 laminates with thickness of 0.87 (B), 1.14 (C), 1.79 (D), 2.21 (E), 4.28 (F) and 8.57 (G) μm, respectively .

SEM (FEI XL30 ESEM-FEG) was used to compare the morphology and the thickness of the laminates, as shown in Figure S4. We did not observe any inclusion of g-C_3N_4 nanosheets in the alumina disk as its pore size is only 0.02μm, nearly one order smaller than the g-C_3N_4 flake size (several hundred of nms, Figure S2).

S2.6 Transmission electron microscopy (TEM)

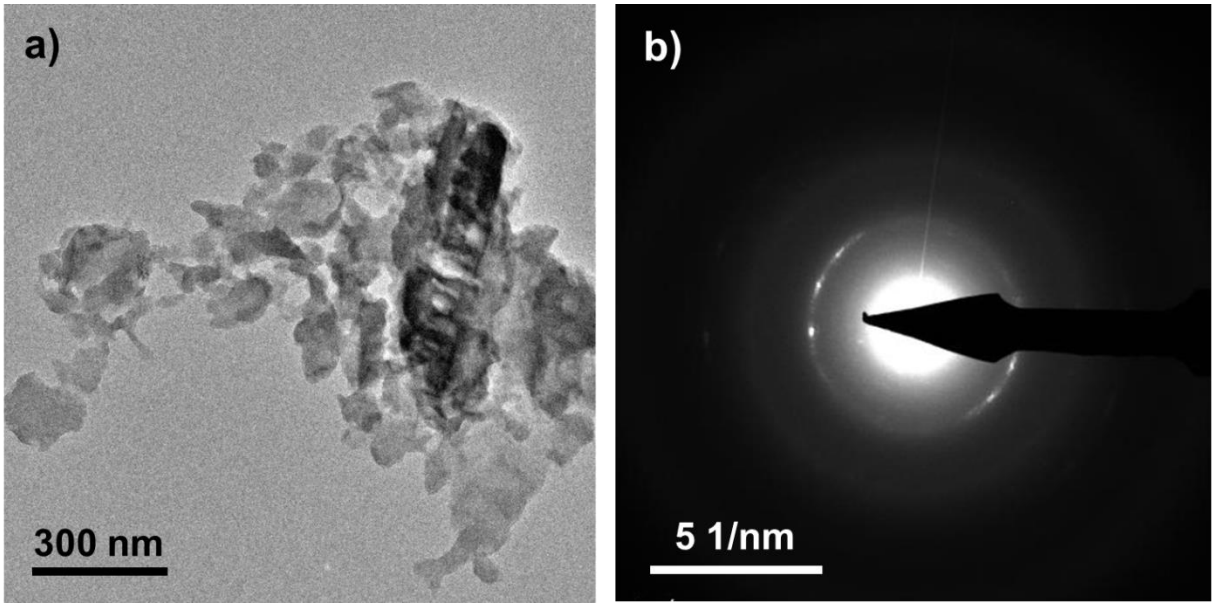

Figure S5. TEM images of g-C_3N_4 sheet (a) and the selected area electron diffraction (SAED) pattern (b) acquired by a FEI Titan 80/200 ChemiSTEM operating at an acceleration voltage of 200 kV.

In the TEM images (Figure S5a), the planar size of the g-C_3N_4 sheets are a few hundred nanometers, similar to the results of AFM in Figure S2. However, we have not observed the hexagonal pattern in the SAED images (Figure S5b), indicating the disordered nature of the nanosheets. The strong reflections observed in the SAED pattern correspond to the (002) lattice spacing, as observed by XRD in Figure 2a.

S2.7 Infrared Spectroscopy

Infrared (IR) spectra were recorded with a Thermo Scientific Nicolet iS5 FT-IR spectrometer with an attenuated total reflectance (ATR) accessory. Each sample was scanned 16 times at a resolution of 4 cm^{-1}. The g-C_3N_4 bulk, LPE sheet and the membrane fabricated by vaccum filtration have nearly identical IR absorption band (Figure S6), indicating that no change in structure due to covalent functionalization is induced in the LPE process.

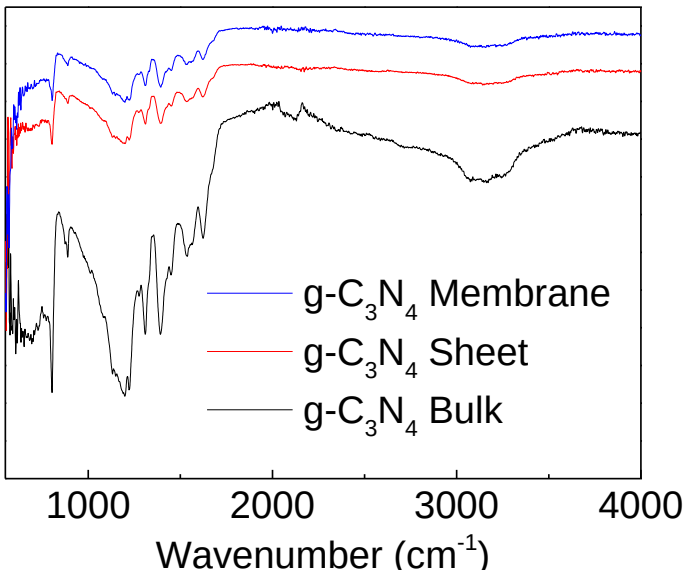

Figure S6. Reflective IR spectra of g-C_3N_4 bulk, LPE nanosheets and the membrane fabricated by vaccum filtration.

S3. Photo-degradation experiments

S3.1 Experimental Process

In this work, we applied three different methods to investigate photo-degradation of organic pollutants in water. All the dyes were purchased from Sigma Aldrich Inc.

i) "Classic" method, Figure S7 A, being the most used in previous studies. The dyes are dissolved in 50vol% IPA/H_2O firstly, and then 5×10^{-5}M of this solvent mixture was mixed with 0.02mg/mL of catalyst. The weight concentrations of Sudan orange G, Rhodamine 110 and methylene blue were fixed at 10.7, 18.3 and 18.7 ppm, respectively. 10 mL of this mixture was placed in a 15 mL glass vial. The reaction was carried out under a 100 W mercury lamp with magnetic stirring. Every 10 or 20 min, 1mL solution was taken out and filter through the 0.45 µm PTFE membrane (Whatman Inc.). The filtered liquid was then measured by UV-Vis spectroscopy to evaluate the residual dyes in solution. This method has been used to produce the data in Fig S10-12 and Table S2.

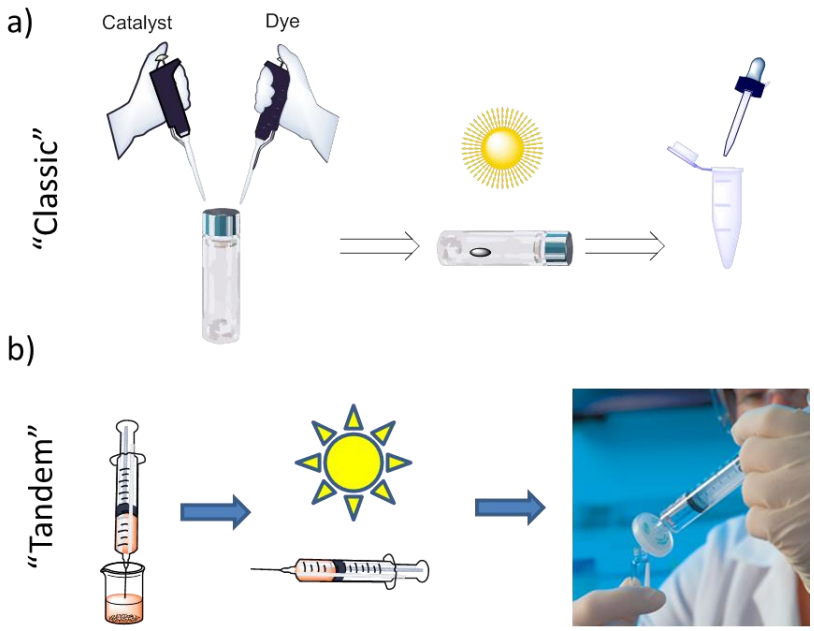

Figure S7 Schematic of: a) "classic" and b) "tandem" process used for photo-degradation studies.

ii) "Tandem" process is a simplified process of the classic process, which includes recycling of the catalysts. The dyes are dissolved in 50vol% IPA/H_2O firstly, and then 5×10^{-5}M of this solvent mixture was mixed with 0.02mg/mL of catalyst. The mixture is then pumped in a plastic syringe (20mL). After placing the syringe under light (100 W, mercury lamp), the solution was filtrated through 0.45 µm PTFE membrane (Whatman Inc.). The UV-vis spectrum of the collected liquid was measured and compared to the initial dye solution. The difference with the classic process is that in this case the catalysis can be recycled from the filter paper and re-dispersed for the next reaction. However, further recycling of the catalyst requires complicated post-treatment, resulting in increased costs.

iii) "2D fixed bed" process (e.g. self-catalytic membrane): here the catalyst is in the form of a laminate and the reactant flow through the pores of the membrane (Figure S8b and 9). This approach is compatible with continuous flux reactors, which are needed industrially. However, the conversion efficiency in this geometry is usually low, as the reactants do not have enough chance to be in contact with the catalysis (Figure S8a). As the space between two g-C_3N_4 nanosheets is close to the size of the dyes, the reactants will have enough chance to engage with the catalyst when flowing through the interlayer space. Furthermore because of the structure of the laminate, the contact area with the catalysts is strongly enhanced, making the catalytic process very efficient, see Figure 3 in main text.

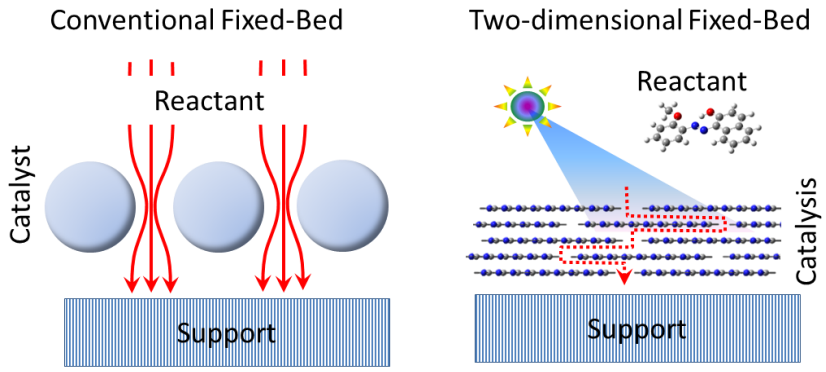

Figure S8 Schematic of: a) traditional fixed bed reactor and b) 2D-nanosheets based reactor for photo-degradation studies.

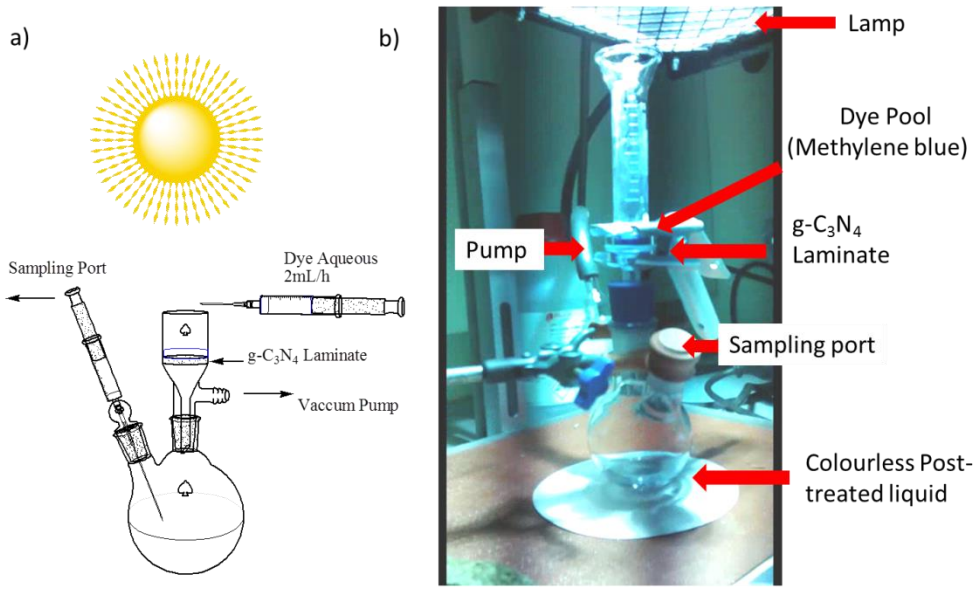

Figure S9 (a) Schematic of the reactor used for the "fixed-bed" process; (b) Picture of the reactor and its components during the photo-degradation experiment.

The "2D fixed bed" process is as following (Figure S9): The fixed-bed catalyst membrane was fabricated by filtrate the dispersion containing 1 mg catalyst was deposited on the anodic alumina oxide paper (0.02µm pore size, 25 mm diameter, Whatsman Inc.). The laminate was characterized by X-ray diffractometer (XRD, RINT2100; Rigaku, Japan) and scanning electron microscope (SEM, FEI XL30 ESEM-FEG). In the photo-degradation, the dye/water solution (5×10^{-5}M) is pumped through the membrane with a flow rate of 2mL/h under a 100 W mercury lamp with a cutoff filter to remove the light below 400nm. The dye residual was evaluated by measuring the absorption spectrum of the mixture after

flowing through the membrane. Noted that the solution above the laminate should not dry, otherwise the laminate will break during the process.

S3.2 Results

S3.2.1 "Classic" process

Figures S10-12 shows the time-evolution of the main absorption peak of SG, MB and Rh during photo-degradation. We compared g-C_3N_4 nanosheets to TiO_2 and bulk g-C_3N_4. Blank experiments (i.e., without catalyst) have been performed for comparison.

The catalytic degradation is a pseudo first-order reaction, therefore the kinetics rate satisfies the following law: $ln(C(t)/C(0)= -Kt$, where $C(0)$ represents the starting concentration of the organic pollutant, $C(t)$ is the concentration of the pollutant at a certain time and K is the kinetic constant, which is proportional to the degradation efficiency. Based on Lambert-Beer Law, we can replace $C(t)$ by the absorbance (measured at 433 nm for SG, at 499 nm for Rh and 664 nm for MB, Figures S10-12).

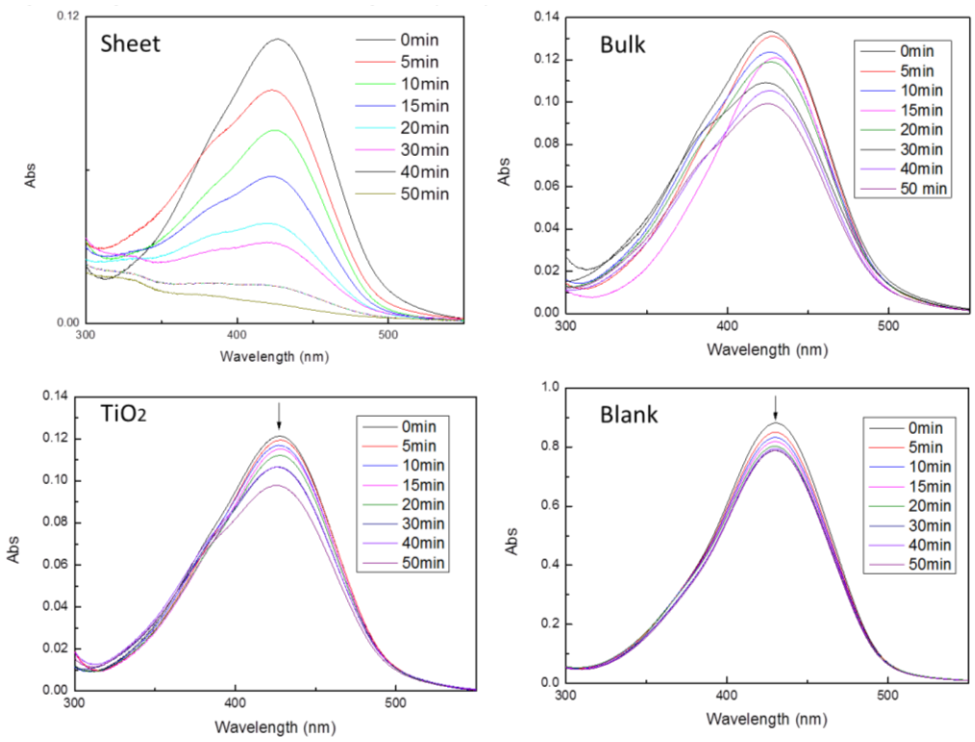

Figure S10 Time-dependent UV-Vis spectra of Sudan orange G after photo-degradation using different photocatalysis.

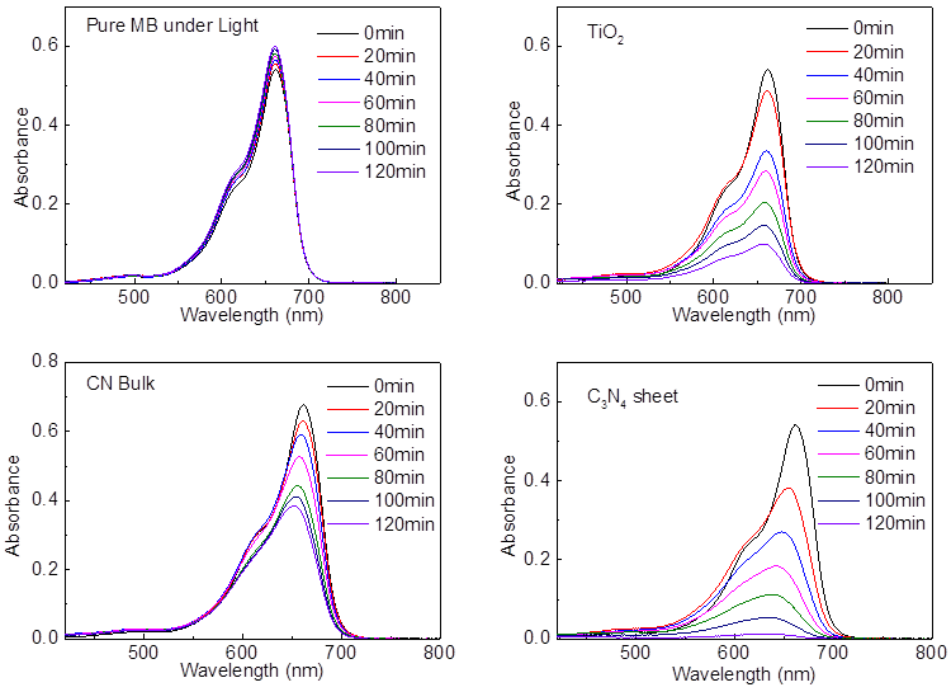

Figure S11 Time-dependent UV-vis spectra of methylene blue after photo-degradation using different photocatalysis.

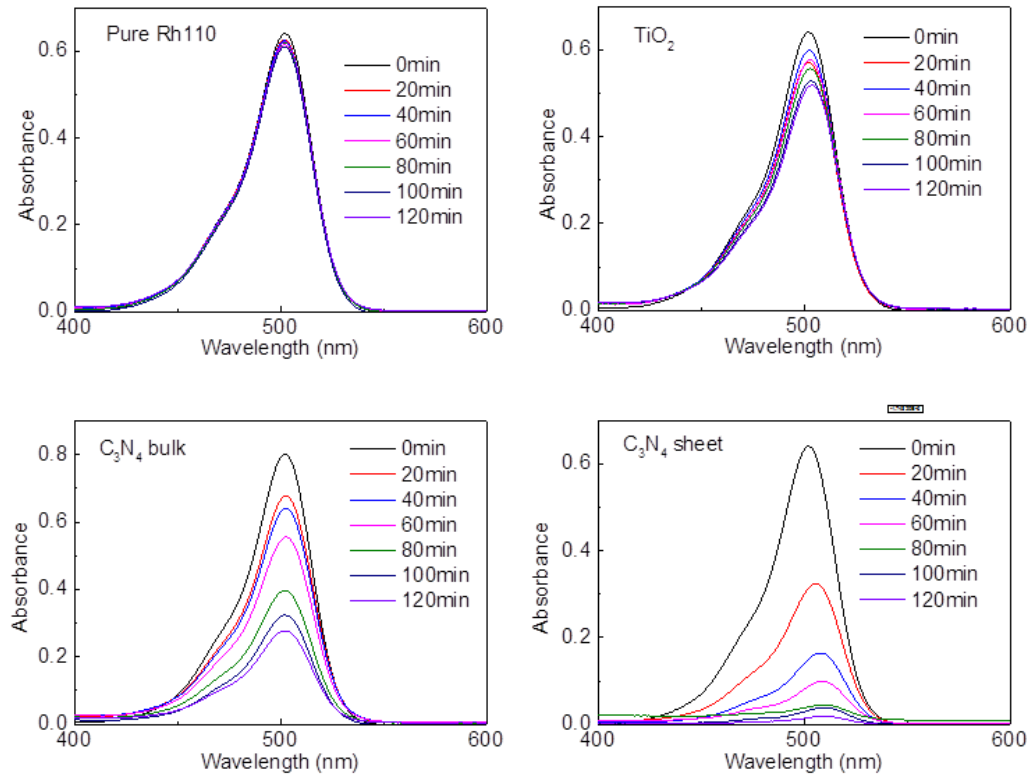

Figure S12 Time-dependent UV-Vis spectra of Rh in the dispersions using different photocatalysis.

Figure S13 shows the changes in concentration as a function of time for the mixture without any catalyst (blank) and by using different catalysts. The plot is linear, as expected from a pseudo first-order reaction, but the slope strongly increases when g-C_3N_4 nanosheets are used. This correlates with an increase in the kinetic constant *k,* showing that g-C_3N_4 nanosheets have the highest photo-catalytic. By fitting the data in Figure S12, we find that the kinetic constant of g-C_3N_4 nanosheets is at least one order of magnitude higher compared to the other catalysts, including bulk g-C_3N_4 (Table S2). In particular, for TiO_2 we found a rather low K, which confirms that this catalyst does not work well under visible light. We found that over 99% of SG is degraded after 60 mins, while the same percentage of MB and Rh is degraded after 100 and 80 mins, respectively.

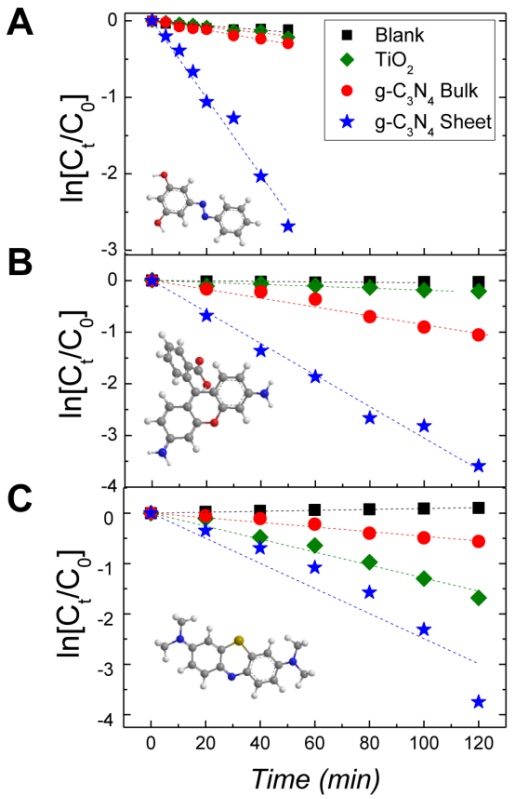

Figure S13. Degradation rate of Sudan Red G, Rhodanine 110 and Methylene Blue (from top to bottom panel) by using different catalysts. The dotted lines are fitted by $ln(C(t)/C_0)= -Kt$. Nanosheets of g-C_3N_4 show in all cases the higher kinetic rate (given by the slope).

We note that MB shows a different behavior compared to Rh and SG. This may be related to the particular photo-degradation mechanism of MB, based on a two-step reaction where the methyl is first removed, and the aromatic skeleton is then decomposed. As the de-methyl compound still have the

same aromatic skeleton, showing similar UV-vis absorption, the apparent conversion efficiency of MB may be underestimated by the UV-absorption.

Table S2 Kinetic rate for degradation of Sudan Orange (SG), Rhodamine 110 (Rh) and Methylene Blue (MB) dissolved in water by using different catalysts. In all cases g-C_3N_4 nanosheets show higher kinetic rate.

	Kinetic rate (hrs^{-1})		
	SG	**Rh**	**MB**
Blank	-0.178	-0.0212	-0.0547
TiO_2	-0.236	-0.107	-0.774
g-C_3N_4 Bulk	-0.362	-0.505	-0.276
g-C_3N_4 Sheet	-3.03	-1.82	-1.38

.

S3.2.2 "Tandem" process

Here we present a practical process to degrade organic pollutants modeled by SG. The pre-mixed SG and g-C_3N_4 nanosheets dispersion was firstly pumped in a syringe. Then, the syringe was placed under visible light for 50 min following the same condition used in Figure S7A. Afterwards, the liquid was manually pumped through 0.45 µm PTFE syringe filter and the filtered liquid analyzed by absorption spectroscopy. Figure S14 shows the UV-vis spectrum of SG before and after 50 minutes "tandem" process. We found that after filtration the residual SG was less than 0.8 % and we did not observe the typical absorption peak of g-C_3N_4 in the 300-450 nm spectral range, indicating that most of catalyst is blocked by the filter paper. Thus, one can easily recycle the nanosheets by removing them from the filter.

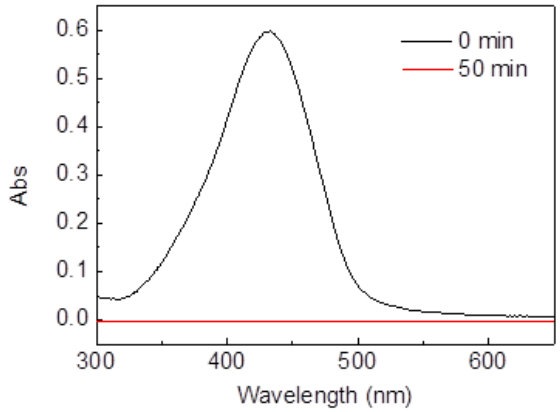

Figure S14 The UV-vis spectrum of SG before and after 50 mins "tandem" process.

S3.2.2 Control experiments (self-catalytic membrane)

In order to confirm that the change in concentration after the liquid flows through the membrane is related to a photo-degradation reaction happening in the laminate and not just to physisorption, we carried a control experiment, where we filtered 2 samples under the same experimental conditions, but one was processed under dark conditions. We measured the absorption spectrum of the liquid that went through the laminate for 2 hrs under dark condition and found that only 5.4% SG dye was trapped in the laminate (Figure S15a), which is very low compared to the decrease in concentration shown in Figure 3c, main text. Therefore, the strong decrease in concentration must be attributed to the photo-degradation effect, not to simple adsorption.

In addition, we also replaced the g-C_3N_4 laminate with the same amount of g-C_3N_4 bulk. 1mg of g-C_3N_4 bulk was stirred with 10 mL 50% IPA/H_2O for 1 hr. Then, the suspension was filtrated by the same method described in section 1.3. The dyes were then pumped through the cake of g-C_3N_4 bulk under light as done in section 3.1. The bulk only degraded ~6 % SG, as the dye just flow through the surface, like in conventional fixed-bed reactor (Figure S8a). This shows that by imposing the liquid to flow through the interlayer space of a nanosheets based membrane, the overall catalytic efficiency can be significantly increased.

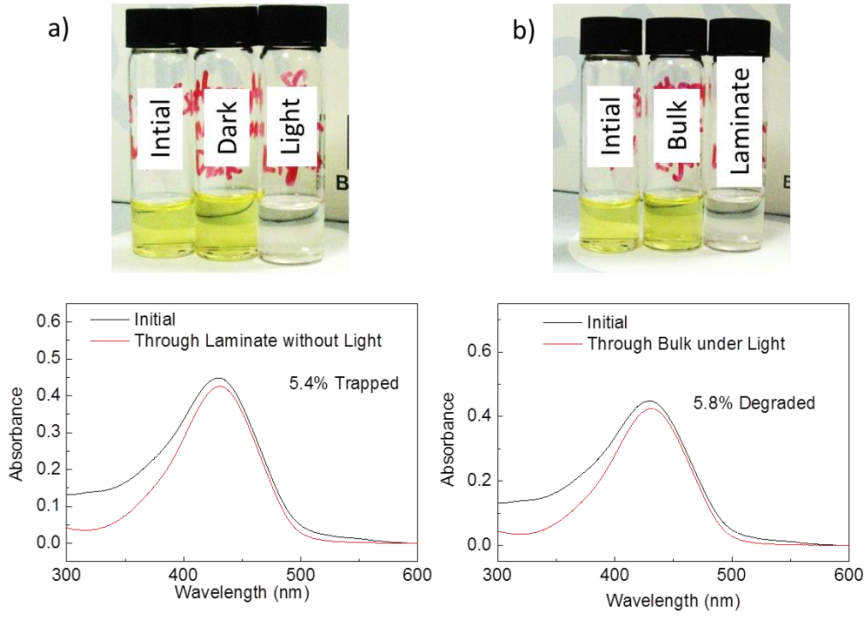

Figure S15 (a) control experiment under dark and light conditions for g-C_3N_4 membranes; (b) comparison between g-C_3N_4 bulk and laminate.

Furthermore, we also produced a laminate by drop casting. The dispersion of g-C_3N_4 sheets was drop casted on the alumina oxide filter, and dried overnight at room temperature. Figure S16 show a SEM image of the film obtained. The structure is more disordered compared to the membrane obtained by vacuum filtration and also shows some cracks probably due to the slow solvent evaporation. We then repeated the photo-degradation process as done in section 3.1. We found that only 56% SG were degraded, in contrast to ≥99% obtained by using the laminate produced by vacuum filtration. This shows that drop casting may be used to produce g-C_3N_4 laminates for photo-degradation experiments, but one has to be careful of the morphology of the laminate.

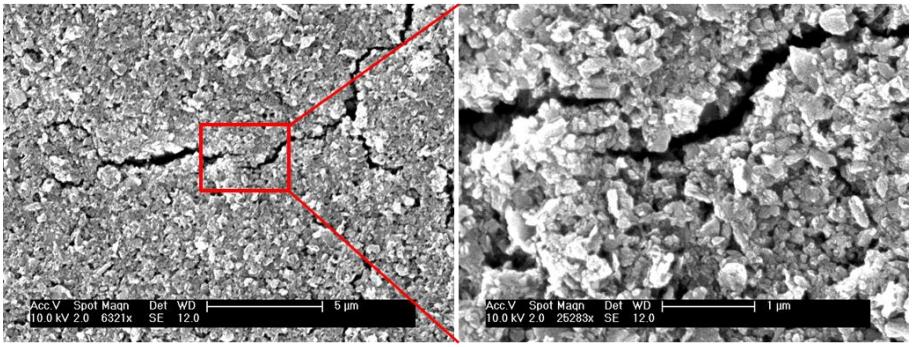

Figure S16 SEM images of the drop-casted films - tiny cracks are visible probably due to solvent evaporation.

S3.2.3 Thickness effect

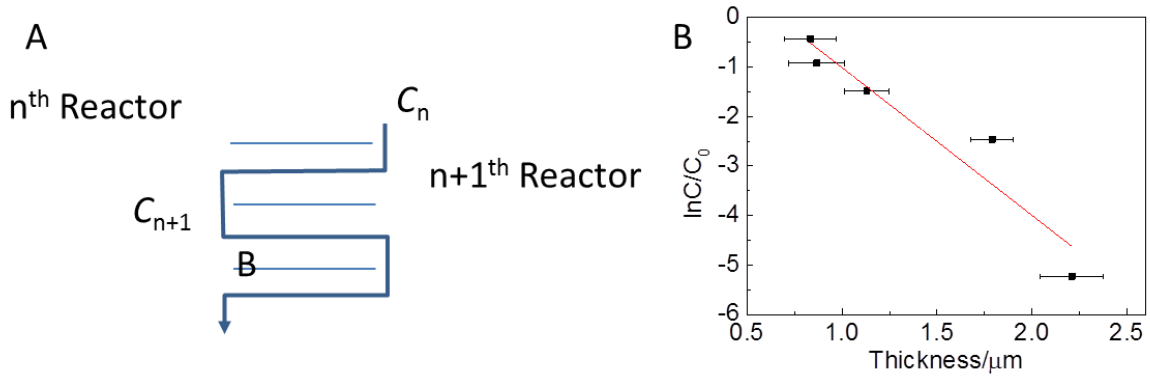

Figure S17 a) schematic of the model based on series of reactors. b) Change in the concentration of SG after 2 hrs as a function of the laminate thickness.

We have shown that membranes based on g-C_3N_4 catalysts show superior catalytic efficiency. This has been attributed to the higher probability of the dye to interact with the active sites while traveling in the interlayer space of the laminate. Under this assumption, we expect the kinetic rate to be dependent of the laminate's thickness. Therefore, we performed photo-degradation experiments on membranes of different thickness (~0.8-2µm). It should also be noted that thin membranes are more fragile, and therefore they can be easily broken. This is why we could not perform experiments below 0.8µm thickness.

To simulate the reaction through the laminate, in first approximation we can use a simple model based on series of reactors. Because of the packing and/or tilting, there is some space left between layers, which can be seen as a nano-reactor, so we can treat the laminate as a group of reactor in series as shown in Fig. S17a. Considering that the photo-degradation process is a first order reaction, the dye concentration after the $(n+1)^{th}$ reactor can be written as:

$$lnC_{n+1} - lnC_n = -kt_{n+1} \quad (7)$$

where the t_{n+1} is the residence time in the $(n+1)^{th}$ reactor, describing the amount of time the fluid has spent inside the reactor. If we sum for the whole series reactors,

$$\sum_{i=1}^{n} (lnC_n - lnC_{n-1}) = -k \sum_{i=0}^{n} t_0$$

then, we can obtain:

$$lnC_n - lnC_0 = -k \sum_{i=0}^{n} t_0 \quad (8)$$

If we let the total residence time as t, then we get :

$$lnC - lnC_0 = -kt \quad (9)$$

where C_0 is the initial concentration of the dye and t is the total residence time in the whole laminate. If we assume the mobility of dye molecules in the laminate to be independent on the thickness, then we can change the Eq. 9 into:

$$\ln(C/C_0) = -k'd \quad (10)$$

where d is the thickness of laminate, and *k'* is the kinetic rate multiplied by the mobility of dyes in the laminate. Following this model the changes in concentration of the dye should be linearly proportional to the thickness of the laminate. We found a good agreement with the experimental results, Fig S17b, considering the simple model used. Therefore, one can tune the thickness of laminate to obtain the wanted conversion rate. Using the model of series reactor, we can further understand the high efficiency of the laminate. In the design of series reactor, large number of small volume reactors in series would obtain higher conversion efficiency than few big volume reactors in series. In the same weight, the packed bulk can be seen as a few reactors with big volume between large particles; meanwhile, the laminate creates more reactors with small volume between layers.

S3.2.3 Photodegradation of Organic Dyes with Membrane Photo-reactor (MPR) at short times

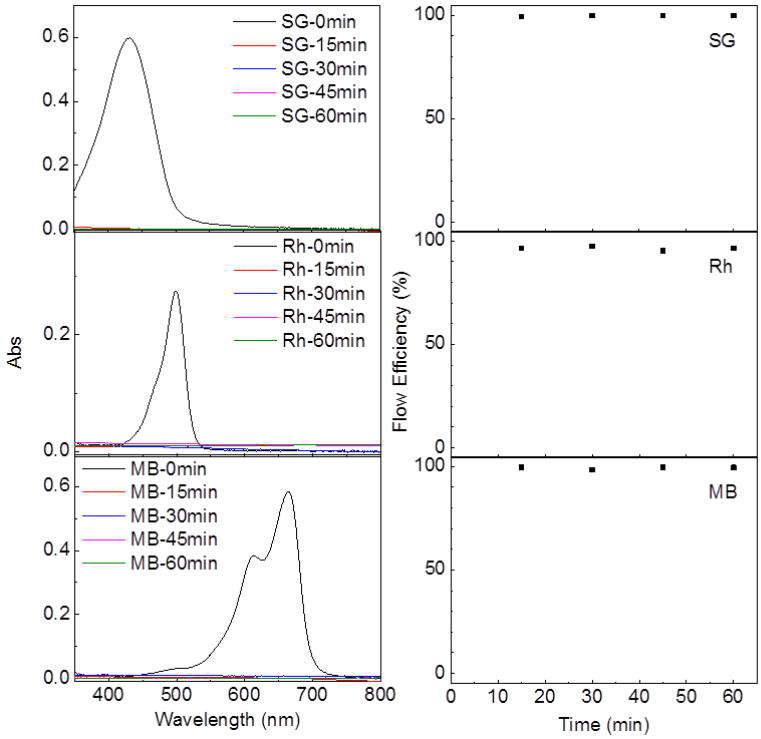

Figure S18 Time-evolution of the UV-Vis spectra for all three dyes investigated: sudan orange G (SG), Rhodamine 110 (Rh) and methylene blue (MB).

Flow efficiency measured within one hour for different organic pollutants. The degradation efficiency of the g-C_3N_4 membrane reactor is always 100%, no matter the reaction time. This is very different from the experiments in solution ("classic process"), where we observed that the g-C_3N_4 dispersion needs 60, 100, and 80 min to totally degrade SG, RhB and MB, respectively (Fig. S12). The efficiency of the

membrane reactor depends on the time required for mass transport through the membrane. Therefore, the thickness of the membrane affects the reaction time: the degradation efficiency increases with the thickness (Fig. 5b). Time-dependent measurements with the fixed-bed membranes were performed to confirm that the membrane efficiency is stable with time, i.e. no changes in the structure of the memebranes or blocking of the pores is observed.

S3.2.4 pH effects on the Membrane Photo-reactor (MPR)

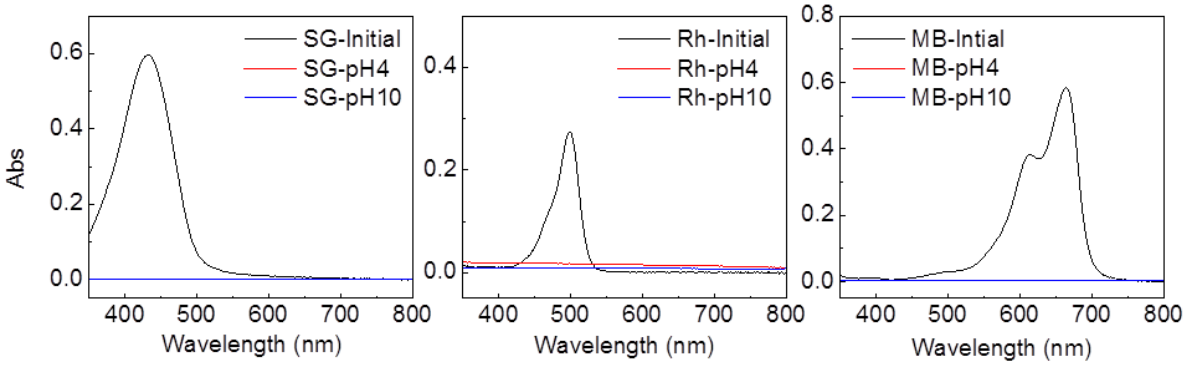

Figure S19 The pH-dependant UV-Vis spectra for all three dyes investigated: sudan orange G (SG), Rhodamine 110 (Rh) and methylene blue (MB) after two hours.

Figure S19 shows the pH-dependant UV-Vis spectra for all three dyes investigated: sudan orange G (SG), Rhodamine 110 (Rh) and methylene blue (MB) after two hours. pH 4 was obtained by addition NaAc/HAc buffer solution to 0.01M, and pH 10 was obtained by addition borax/sodium hydroxide buffer solution. pH effects on the photodegradation are very complicated, as shown for previous particle catalysts.[8-9] Firstly, owing to the negative charge on the catalytic surface, the absorption of a positively charged dye or metal ion will be enhanced at low pH, leading an increasing in degradation efficiency.[9] Secondly, hydroxyl radicals are generated more readily in alkaline solution, thus the efficiency of the process is logically enhanced.[10] On the other hand, the Columbic repulsion between the surface and hydroxide anions at high pH would decrease the efficiency to generate ·OH radical species, and consequently reduce the photodegradation performance.[8] However, in our MPR, the reaction has been restricted in a small space. As a result, absorption and electrostatic repulsion has less effect compared to the spatial restriction. Therefore, the pH has little effect on the photodegradation as shown in Figure S19.

References

[1] a) Y. Hernandez, V. Nicolosi, M. Lotya, F. M. Blighe, Z. Sun, S. De, I. T. McGovern, B. Holland, M. Byrne, Y. K. Gun'Ko, J. J. Boland, P. Niraj, G. Duesberg, S. Krishnamurthy, R. Goodhue, J. Hutchison, V. Scardaci, A. C. Ferrari, J. N. Coleman, *Nat. Nanotech.* **2008**, *3*, 563-568; b) G. Cunningham, M. Lotya, C. S. Cucinotta, S. Sanvito, S. D. Bergin, R. Menzel, M. S. P. Shaffer, J. N. Coleman, *ACS Nano* **2012**, *6*, 3468-3480; c) J. N. Coleman, M. Lotya, A. O'Neill, S. D. Bergin, P. J.

King, U. Khan, K. Young, A. Gaucher, S. De, R. J. Smith, I. V. Shvets, S. K. Arora, G. Stanton, H.-Y. Kim, K. Lee, G. T. Kim, G. S. Duesberg, T. Hallam, J. J. Boland, J. J. Wang, J. F. Donegan, J. C. Grunlan, G. Moriarty, A. Shmeliov, R. J. Nicholls, J. M. Perkins, E. M. Grieveson, K. Theuwissen, D. W. McComb, P. D. Nellist, V. Nicolosi, *Science* **2011**, *331*, 568-571.

[2] K.-G. Zhou, N.-N. Mao, H.-X. Wang, Y. Peng, H.-L. Zhang, *Angew. Chem. Int. Ed.* **2012**, *50*, 10839-10842.

[3] Y. Hernandez, M. Lotya, D. Rickard, S. D. Bergin, J. N. Coleman, *Langmuir* **2009**, *26*, 3208-3213.

[4] S. C. Yan, Z. S. Li, Z. G. Zou, *Langmuir* **2009**, *25*, 10397-10401.

[5] X. Wang, K. Maeda, A. Thomas, K. Takanabe, G. Xin, J. M. Carlsson, K. Domen, M. Antonietti, *Nat. Mater.* **2009**, *8*, 76-80.

[6] S. Ono, T. Funato, Y. Inoue, T. Munechika, T. Yoshimura, H. Morita, S.-I. Rengakuji, C. Shimasaki, *J. Chromatogr. A* **1998**, *815*, 197-204.

[7] B. Jürgens, E. Irran, J. Senker, P. Kroll, H. Müller, W. Schnick, *J. Am. Chem. Soc.* **2003**, *125*, 10288-10300.

[8] I. K. Konstantinou, T. A. Albanis, *Applied Catalysis B: Environmental* **2004**, *49*, 1-14.

[9] a) V. K. Gupta, R. Jain, T. A. Saleh, A. Nayak, S. Malathi, S. Agarwal, *Separation Science and Technology* **2011**, *46*, 839-846; b) T. A. Saleh, *Desalination and Water Treatment* **2016**, *57*, 10730-10744; c) T. A. Saleh, *Environmental Science and Pollution Research* **2015**, *22*, 16721-16731; d) T. A. Saleh, V. K. Gupta, *Environmental Science and Pollution Research* **2011**, *19*, 1224-1228.

[10] C. Galindo, P. Jacques, A. Kalt, *Journal of Photochemistry and Photobiology A: Chemistry* **2000**, *130*, 35-47.